Chinese Journal of
POLYMER SCIENCE

RESEARCH ARTICLE

https://doi.org/10.1007/s10118-022-2866-2
Chinese J. Polym. Sci. **2023**, *41*, 842–850

The Role of Processing Solvent on Morphology Optimization for Slot-Die Printed Organic Photovoltaics

Lei Wang[a], Jun-Zhe Zhan[a], Wen-Kai Zhong[b], Lei Zhu[b*], Guan-Qing Zhou[b], Tian-Yu Hao[b], Ye-Cheng Zou[c], Zhen-Hua Wang[c], Gang Wei[c], Yong-Ming Zhang[b], and Feng Liu[a,b*]

[a] *School of Physics and Astronomy, Shanghai Jiao Tong University, Shanghai 200240, China*
[b] *Frontiers Science Center for Transformative Molecules, Center of Hydrogen Science, School of Chemistry and Chemical Engineering, Shanghai Jiao Tong University, Shanghai 200240, China*
[c] *State Key Laboratory of Fluorinated Functional Membrane Materials and Dongyue Future Hydrogen Energy Materials Company, Zibo 256401, China*

Electronic Supplementary Information

Abstract The morphology manipulation of the active layers is important for improving the performance of organic photovoltaics (OPVs). The choice of processing solvent has great impact on the crystallization and phase separation during film formation, since solvent properties, including solvent effect on molecular crystallization, boiling point, and interaction parameters, can directly change the evolution pathways associated with thermodynamics and kinetics. Therefore, revealing the underlying solvent-regulated morphology mechanism is potential to provide guiding strategies for device optimization. In this study, chloroform, chlorobenzene, and toluene are used to process PM6:Y6 blends by slot-die printing to fabricate OPV devices. The chloroform printed film forms a fibrillar network morphology with enhanced crystallization, facilitating exciton dissociation, charge transport and extraction, resulting in an optimal power conversion efficiency of 16.22%. However, the addition of the additive chloronaphthalene in chloroform solution leads to over-crystallization of Y6, and thus, increasing domain size that exceeds the exciton diffusion length, resulting in lower device efficiency. In addition, both the chlorobenzene and toluene suppress the crystallization of Y6, which drastically decreased short-circuit current and fill factor. These results demonstrate the important role of processing solvent in dictating film morphology, which critically connects with the resultant printed OPV performance.

Keywords Organic solar cells; Morphology; Processing solvent; Crystallization; Phase separation

Citation: Wang, L.; Zhan, J. Z.; Zhong, W. K.; Zhu, L.; Zhou, G. Q.; Hao, T. Y.; Zou, Y. C.; Wang, Z. H.; Wei, G.; Zhang, Y. M.; Liu, F. The role of processing solvent on morphology optimization for slot-die printed organic photovoltaics. *Chinese J. Polym. Sci.* **2023**, *41*, 842–850.

INTRODUCTION

Organic photovoltaics (OPVs) aroused broad interest from academia and industry in the past few decades, since such emerging solar technology is potential to assist in the realization of net zero emissions and wearable electronics.[1–3] To this end, large-area roll-to-roll (R2R) film printing is one of the inevitable challenges that must be tackled by the OPV sector. Despite single-junction devices achieving high efficiencies over 19%,[4,5] OPV fabrications in laboratory deeply rely on spin-coating, where the solution drying is much faster than R2R printing, leading to different crystallization and phase separation kinetics during film formation. Thus, the optimized processing conditions obtained by spin-coating cannot be directly transferred to R2R printing. To circumvent such problem, using slot-die printing for film processing is an appropriate option to understand the structure-function relations, which provides optimized processing conditions that are more favorable for industrial manufacturing.[6–9] However, the reported power conversion efficiencies (PCEs) of slot-die printed devices are usually lower than spin-coated devices due to the difficulty in controlling the thin film deposition.[10,11] Thus, effective strategies have been explored to optimize the morphology, such as processing solvent,[12–14] solvent additive,[15–17] ternary strategy,[18,19] thermal annealing,[20] *etc*. The interactions between solvent and materials will affect the aggregation state of materials in solution, and the boiling point of the solvent determines the drying rate of the film as well as the termination of morphology evolutions. Understanding the solvent properties, such as boiling point and interaction parameters with material, is essential to obtain high-performance devices. Shin and colleagues found that PCDTBT:$PC_{71}BM$ films spin-coated from chlorobenzene (CB) or chloroform (CF) showed large aggregate structures, while no aggregates were observed in those spin-coated from dichlorobenzene (DCB), due to the higher solubility of $PC_{71}BM$ in DCB.[21] Ruderer and colleagues prepared P3HT:$PC_{61}BM$ blend films by different processing

* Corresponding authors, E-mail: zhulei1130@outlook.com (L.Z.)
E-mail: fengliu82@sjtu.edu.cn (F.L.)

Received June 26, 2022; Accepted September 6, 2022; Published online October 20, 2022

solvents (CF, CB, toluene and xylene).[22] Morphological analysis showed that the grain size of P3HT increased with solvent boiling point increasing, since a high boiling point could prolong drying process, providing sufficient time for the self-assembly of polymer chains during solvent evaporation. Liu and colleagues investigated the effects of solvent and thermal annealing on the morphology of PM6:Y6 films. They found that a proper choice of processing solvent could drive the formation of polymer-like assembly stacks of Y6 molecules, which can further develop into 2D transport networks that substantially improve device charge transport.[23] Ma and colleagues investigated the effect of miscibility on the morphology during slot-die processing with different solvents. They found that in the low-miscibility D18:Y6 system, incorporating a trace amount of CB into CF causes a significant aggregation of Y6.[11] However, most studies on processing solvents focused on the morphology optimization of spin-coated active layers, while few reports discussed the effect of solvents on the morphology manipulation of printed photoactive layers. Therefore, a thorough understanding of the solvent effects on the morphology of printed films needs to be explored to accelerate the transfer of technology from laboratory fabrication to industrial production.

In this work, a high-efficiency OPV blend system, PM6:Y6, is used to investigate the role of processing solvent in manipulating the film morphology resulted from slot-die printing. Different processing solvents are employed, including CF, CF with 0.5 vol% chloronaphthalene (CN), CB, and toluene (TO). The morphology is highly dependent on the solvent effects on solutes crystallization, evaporation rate, and the interaction parameters with solutes. Device physics indicates that exciton dissociation, charge transport, and charge extraction of devices are in connection with morphological tunning. The CF-processed PM6:Y6 film forms a fibrillar morphology with proper phase separation length scales, exhibiting an optimal PCE of 16.22%. These results provide new insight into the role of processing solvent for the preparation of printed OPV devices.

EXPERIMENTAL

Experimental section is in the electronic supplementary information (ESI).

RESULTS AND DISCUSSION

Devices were fabricated with an architecture of ITO/PEDOT:PSS/PM6:Y6/PFN-Br/Ag. The chemical structures of PM6 (donor) and Y6 (acceptor) are shown in Fig. 1(a). Shown in Fig. 1(b) are the UV-Vis absorption spectra of PM6:Y6 blended films processed with different solvents. All films have distinct absorption peaks around 630 and 820 nm, which are contributed by PM6 and Y6, respectively. The spectral complementarity of PM6 and Y6 covers a broad absorption range from visible to near-infrared region. The current density-voltage (*J-V*) curves are shown in Fig. 1(c) and the detailed device parameters are summarized in Table 1. The V_{OC} of CF-processed device is 0.84 V, which is higher than the CF/CN-, CB-, and TO-processed devices with V_{OC} of 0.83, 0.79 and 0.79 V, respectively. The optimal PCE of 16.22% are obtained for the blends processed with CF, while the PCE decreases to 12.3% for blends processed with CF/CN, mainly due to the drop in short-circuit current density (J_{SC}) and fill factor (FF). When the blends are processed with CB and TO, all parameters decreased, especially J_{SC} (16.35 and 9.45 mA·cm^{-2}) and FF (54.85% and 55.34%), resulting in low PCEs of 7.08% and 4.15%, respectively. The external quantum efficiency (EQE)

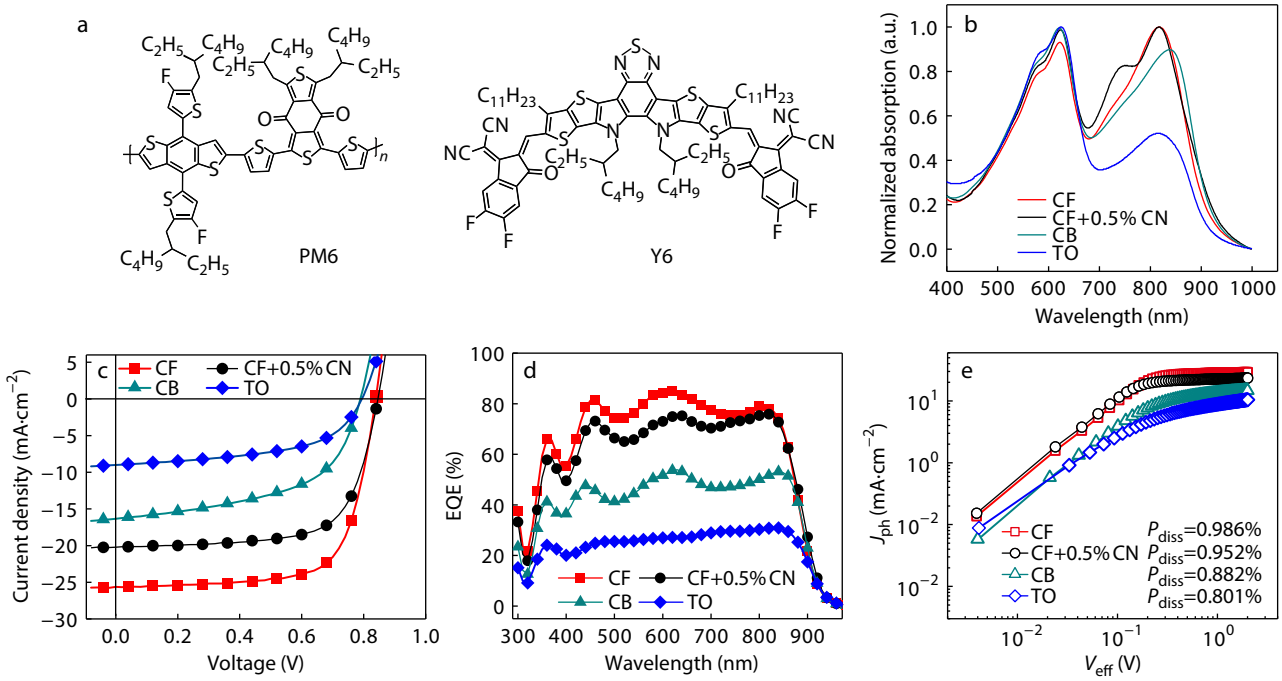

Fig. 1 (a) Chemical structures of PM6 and Y6; (b) Normalized UV-Vis absorption spectra of PM6-Y6 blend films processed by different solvents; (c) *J-V* curves, (d) EQE curves, and (e) J_{ph}-V_{eff} of the PM6:Y6-based devices processed with different solvents.

https://doi.org/10.1007/s10118-022-2866-2

Table 1 Solar cell device parameters of PM6:Y6 blends processed with different solvents.

Solvents	V_{OC} [a] (V)	J_{SC} [a] (mA·cm^{-2})	FF [a] (%)	PCE [a] (%)	J_{SC} [b] (mA·cm^{-2})
CF	0.84±0.01 (0.84)	25.12±0.54 (25.6)	74.17±1.50 (75.46)	15.95±0.30 (16.22)	24.93
CF+CN	0.83±0.01 (0.83)	22.52±0.43 (23.17)	62.10±1.90 (64.15)	11.89±0.45 (12.30)	22.24
CB	0.79±0.01 (0.79)	15.95±0.50 (16.35)	53.91±1.30 (54.85)	6.85±0.25 (7.08)	15.84
TO	0.79±0.01 (0.79)	9.10±0.40 (9.45)	54.21±1.20 (55.34)	3.95±0.19 (4.15)	9.18

[a] Average values calculated from 10 devices (best values in the bracket); [b] J_{SC} integrated from the EQE spectrum.

spectra are shown in Fig. 1(d), in which the CF-processed device shows high values of ~80% in the spectral range of 450–800 nm. CB and TO processing lead to significant decrease of EQEs, suggesting the suppressed charge carrier transport and extraction. The short-circuit current density integrated from EQE curves are 24.93, 22.24, 15.84 and 9.18 mA·cm^{-2} for the devices processed by CF, CF/CN, CB and TO, which are in good agreement with the J_{SC} obtain from the *J-V* measurements with a deviation less than 5%.

Photocurrent density-effective voltage (J_{ph}-V_{eff}) curves of devices were measured to investigate the exciton dissociation and charge collection.[24–26] J_{ph} is defined as $J_{ph} = J_L - J_D$, which represents the difference between the current densities under light illumination and in the dark. V_{eff} is defined as $V_{eff} = V_0 - V_a$, where V_0 is the voltage at J_{ph}=0 and V_a is the applied voltage bias. As shown in Fig. 1(e), the J_{ph} of the device processed with CF shows the highest saturation photocurrent density (J_{sat}), indicating efficient exciton separation and charge collection, in agreement with the high EQEs. Charge collection of the devices is evaluated by J_{SC}/J_{sat}. The J_{SC}/J_{sat} values are 0.986 and 0.952 for PM6:Y6 devices processed by CF and CF/CN, respectively, both of which are higher than those of 0.882 and 0.801 for devices processed by CB and TO, respectively. These results indicate that CF and CF/CN devices display efficient exciton dissociation and charge extraction, which is consistent with high J_{SC} and FF.

The electron-only and hole-only devices were fabricated to extract the hole and electron mobilities of blends by space-charge-limited current (SCLC) method,[27,28] and the corresponding *J-V* curves and fitted mobilities are summarized in Fig. S1 and Table S1 (in ESI), respectively. Charge carrier transport is significantly improved for the CF-processed device with hole mobility (μ_h) and electron mobility (μ_e) of 8.21×10^{-4} and 6.99×10^{-4} cm^2·V^{-1}·s^{-1}, with a mobility ratio (μ_h/μ_e) of 1.17. Thus, the CF-processed blend shows balance transport compared with CF/CN, CB and TO-processed blends with ratios of 1.47, 2.27 and 4.90, respectively. The gradual decrease in mobilities of the blends processed by CF/CN, CB and TO is due to the exacerbated charge recombination loss in corresponding devices, as evidenced by light-intensity dependences of V_{OC} and J_{SC} and TPV/TPC measurements, which will be discussed in the following sections.

Charge transfer kinetics of the PM6:Y6 blends was studied by transient absorption (TA) spectroscopy measurements.[29–32] We selected 800 nm laser to pump acceptor (Y6) only because of the well separated absorption of PM6 and Y6. The 2D color contours of TA spectra of PM6:Y6 blends processed with CF, CF/CN, CB and TO are shown in Figs. 2(a), 2(b), 2(d) and 2(e), respectively. The representative fs-transient absorption spectrum of CF-processed blend is shown in Fig. 2(c). With the decay of Y6 bleach peak at 620–850 nm related with the ground state bleach (GSB) and stimulated emission (SE), a

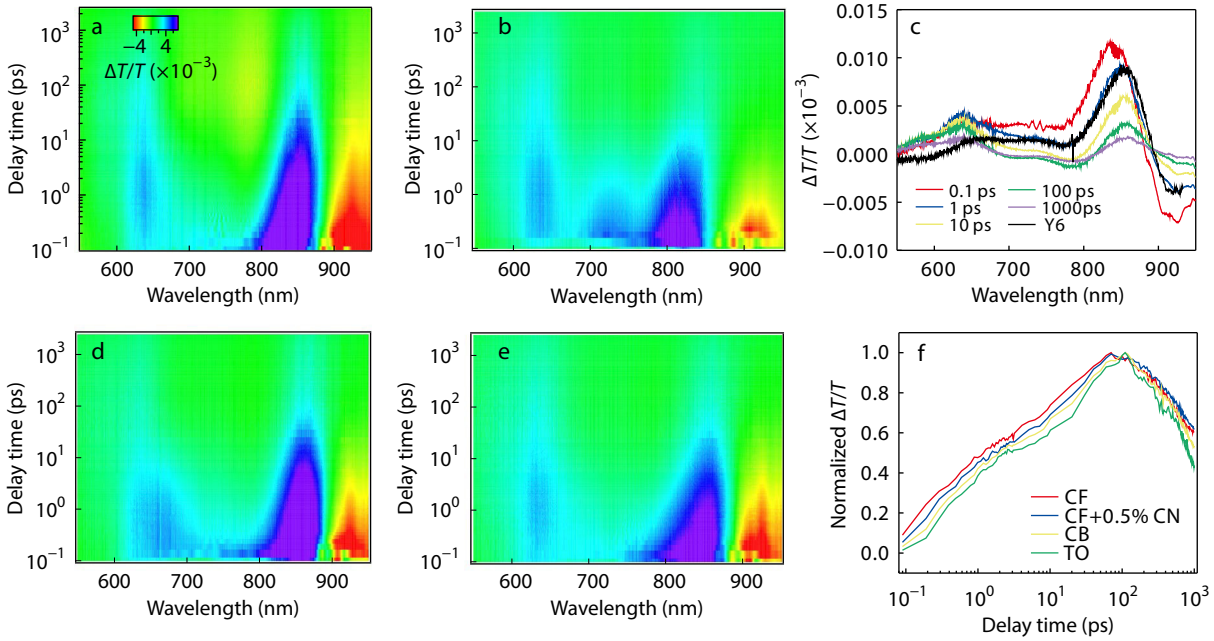

Fig. 2 Color plot of fs-transient absorption spectra of PM6:Y6 blend films processed by (a) CF, (b) CF/CN, (d) CB, and (e) TO at indicated delay times under 800 nm excitation with a fluence below 5 μJ/cm^2. Representative fs-transient absorption spectra of PM6:Y6 blended films processed by (c) CF at indicated delay time. (f) TA kinetics of PM6:Y6 blended films at different conditions indicating of hole transfer process.

https://doi.org/10.1007/s10118-022-2866-2

few clear bleach peaks at 550–600 nm which matched well with the GSB of PM6 appear in the transient absorption spectrum of PM6:Y6 film, confirming photoexcited hole transfer from Y6 to PM6. As presented in Fig. S3 (in ESI), such a hole transfer process also occurred in blend films under the other three conditions. The dynamics of hole transfer process is characterized by two-time scales by fitting the GSB signal of PM6 probed at ~600 nm (Fig. 2f). After biexponential fitting, we found two-time constants are available, where τ_1 could be assigned to be ultrafast exciton dissociation at the donor/acceptor interface and τ_2 represents the diffusion of excitons towards interfaces before dissociation. As shown in Table S2 (in ESI), the hole transfer times of CF-processed film are 0.331 ps and 13.816 ps for τ_1 and τ_2, respectively, which outperform those of the CF/CN-processed film with τ_1 of 0.346 ps and τ_2 of 14.557 ps, indicating optimized distribution of donor/acceptor regions. The CB- and TO-processed films show lower hole transfer rate with τ_1/τ_2 of 0.371/15.361 ps and 0.396/17.72 ps, respectively, which are consistent with the J_{ph}-V_{eff} analysis and the device performance.

As charge carriers will encounter mono- or bi-molecular recombination during transport process, which can be accessed by the light intensity (P_{light}) dependence of V_{OC} and J_{SC} measurements.[33,34] When the slope of $V_{OC} \propto P_{light}$ is equal to kT/q, the bimolecular recombination is the dominant nongeminate recombination mechanism, while a large value more than kT/q indicates that the trap-assisted recombination can be evolved in the devices. As displayed in Fig. S2(a) (in ESI), the slope of CF-processed device is 1.10kT/q, which is lower than the CF/CN-, CB- and TO-processed devices with slopes of 1.38kT/q, 1.68kT/q and 1.71kT/q, respectively. Such results suggest depressed trap-assisted recombination is achieved when the blend film is processed with CF. Besides, we studied the relationship between J_{SC} and P_{light} according to $J_{SC} \propto P_{light}^{\alpha}$, where α is the exponential factor. If the α value is close unity, it indicates low bimolecular recombination in device. As shown in Fig. S2(b) (in ESI), the α value for CF-processed device is 0.987, which is higher than CF/CN-, CB- and TO-processed devices with 0.943, 0.929 and 0.913, respectively. The results indicate that the CF-processed device shows lower bimolecular recombination. The reduced nongeminate recombination in CF-processed device indicates improved semiconducting properties. The CF/CN processed device is dominated by the biomolecular recombination, coupled with slight trap-assisted recombination. Both CB- and TO-processed devices show severe bimolecular recombination and trap-assisted recombination.

Transient photovoltage (TPV) and photocurrent (TPC) measurements were performed to obtain the charge density with their lifetime, which can be used to determine the nongeminate recombination property under different V_{OC} values.[35–37] Fig. 3(a) shows the carrier lifetime versus V_{OC} under different processing conditions. The CF-processed device presents a longer lifetime than those of the CF/CN-, CB-, and TO-processed devices over the probed V_{OC} values, which indicates reduced carrier loss channels and a more efficient carrier extraction to generate current. Fig. 3(b) shows the dependence of carrier lifetime (τ) on charge density (n). All curves exhibit an approximately exponential dependence following $\tau = \tau_0\left(\frac{n_0}{n}\right)^{\lambda}$, where τ_0 and n_0 are constants, and λ is the exponential factor, indicating non-geminate recombination dominates carrier loss in devices.[38] The recombination order R can be calculated by λ ($R = \lambda + 1$). When R is 2, the bimolecular recombination is the dominant non-geminate recombina-

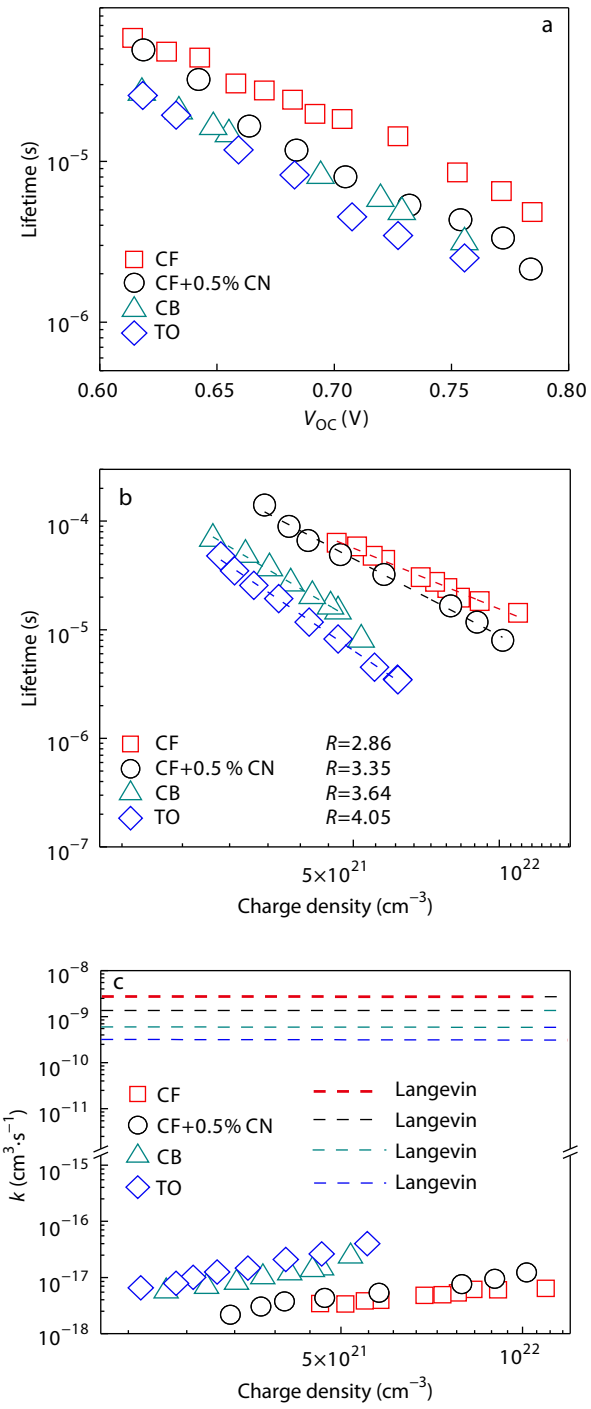

Fig. 3 (a) TPV measurements of the devices; (b) Dashed lines are the liner fits of the measured data points; the recombination orders R is indicated in the graph; (c) Measured nongeminate recombination rate coefficient k for the devices. The dashed lines represent Langevin recombination rate coefficient for the devices processed by different solvents.

tion mechanism, while a higher value of R more than 2 indicates the presence of trap states. By fitting the curves in Fig. 3(b), the values of R in CF-, CF/CN-, CB- and TO-processed devices are 2.86, 3.35, 3.64 and 4.05, respectively. Such results imply that CF-processed device shows the lowest trap density than the devices fabricated by other processing conditions. The non-geminate recombination rate coefficient $k(n)$ can be defined by the equation $k(n) = \frac{1}{\tau(n) \times n}$, where $\tau(n)$ is the total charge carrier lifetime.[39] Fig. 3(c) describes the $k(n)$ as a function of charge density under different processing solvents. The non-geminate recombination rate coefficients of CF- and CF/CN-processed devices are smaller than those of CB- and TO-processed devices, which imply that the devices processed by CF and CF/CN have less non-geminate recombination loss, suggesting a favorable morphology with efficient carrier transport channels. These results are in good agreement with the analysis obtained from light intensity dependence measurements.

The unified analysis of device performance, photophysics, and device physics demonstrates that CF-processed device exhibits faster hole transfer with higher and more balanced carrier mobilities, efficient exciton dissociation and charge collection. The use of CF/CN cannot help to improve the device performance. Both CB- and TO-processed devices show severe non-geminate recombination, suppressed exciton dissociation, carrier transport and extraction, leading to a plunge in both J_{SC} and FF. In order to understand the morphological origins of the different device performance, the details of film morphology were studied.

Grazing incidence wide angle X-ray scattering (GIWAXS) was performed to study crystallization and packing orientations in PM6:Y6 blend films processed by different solvents. Fig. 4 shows the 2D patterns and corresponding cake-averaged curves in the in-plane (IP) and out-of-plane (OOP) directions. The broad peak at ~0.28 Å^{-1} in the IP direction originates from lamellar stacking of materials, *i.e.*, the (100) reflection of PM6 and the (110) reflection of Y6. The π-π stacking signals appear at ~1.72 Å^{-1}, which are also contributed by both PM6 and Y6. CF-processed film shows a strong π-π stacking peak at ~1.72 Å^{-1} in the OOP direction, indicating a preferential face-on orientation. CF/CN-processed film shows stronger π-π stacking reflection, indicative of enhanced face-on orientation. For CB- and TO-processed blends, the π-π stacking peaks are at ~1.70 Å^{-1} with weak and azimuthal spreading characteristics, suggesting the crystalline orientations in the blends are random. As crystalline orientation of PM6 does not change upon processed with different solvents,[23,40,41] the change in crystalline orientation in the PM6:Y6 blends must stem from the change of Y6 crystallization.[42] Such argument can also be evidenced by the CF/CN blend, where the intensified π-π stacking reflection is accompanied with the intense and sharp Y6 (020) and (11-1) diffraction peaks at ~0.21 and ~0.43 Å^{-1} in the IP direction, demonstrating the increased Y6 crystallization help to promote the face-on crystalline packing in blends. And Y6 shows low crystallinity in CB- or TO-processed blends, with weak and random crystalline packing.

Multi-peak fitting the low-q reflections in the IP direction result in d-spacing, peak area, and crystalline coherence length (CCL) associated with lamellar stacking and Y6 (11-1) reflection (Fig. 5 and Table S3 in ESI). The peak areas of the lamellar and Y6 (11-1) peaks of the CF-processed films are larger than those of CB- and TO-processed films, indicating that the CF processing is more favorable for molecular ordering during film drying. It is also observed that substantial increase in CCLs is seen in CF/CN-processed films, which are attributed to the formation of more ordered self-assembly of Y6 molecules under prolonged drying time. The ratio of peak areas between the π-π stacking peaks (q ~1.7 Å^{-1}) and the amorphous peaks (q ~1.3 Å^{-1} for CF- and CF/CN-blends; q ~1.2 Å^{-1} for CB- and TO-blends) can be used to evaluated the

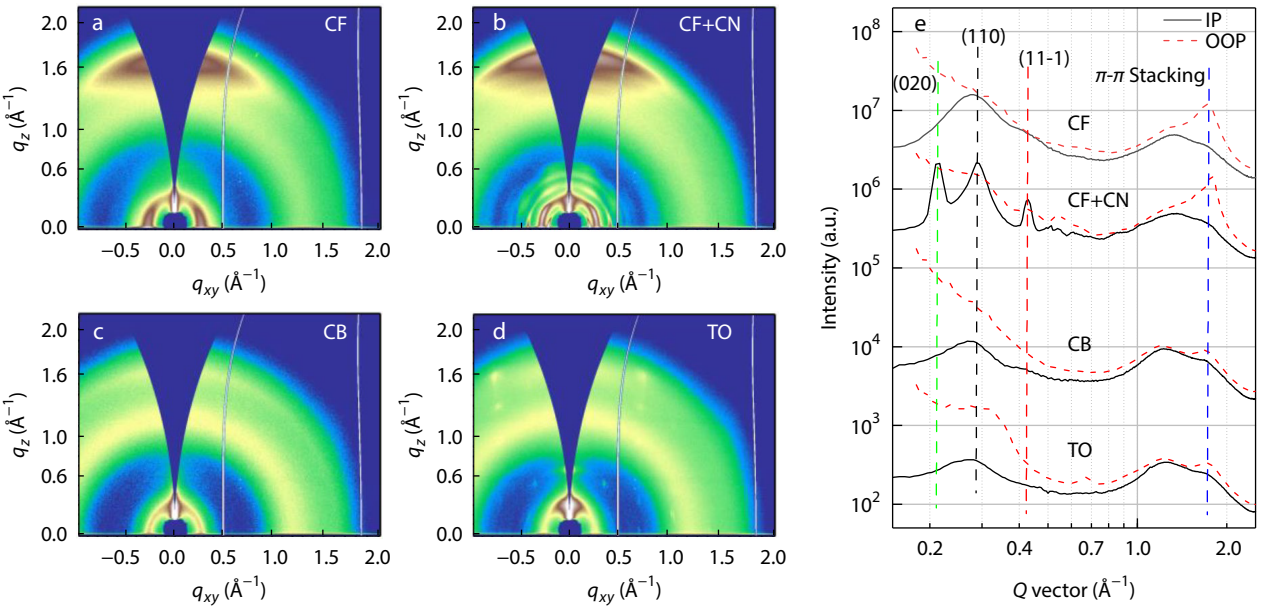

Fig. 4 GIWAXS patterns of PM6:Y6 blend films processed by (a) CF, (b) CF/CN, (c) CB, and (d) TO; (e) Sector-averaged curves in the in-plane (IP, black lines) and out-of-plane (OOP, red lines).

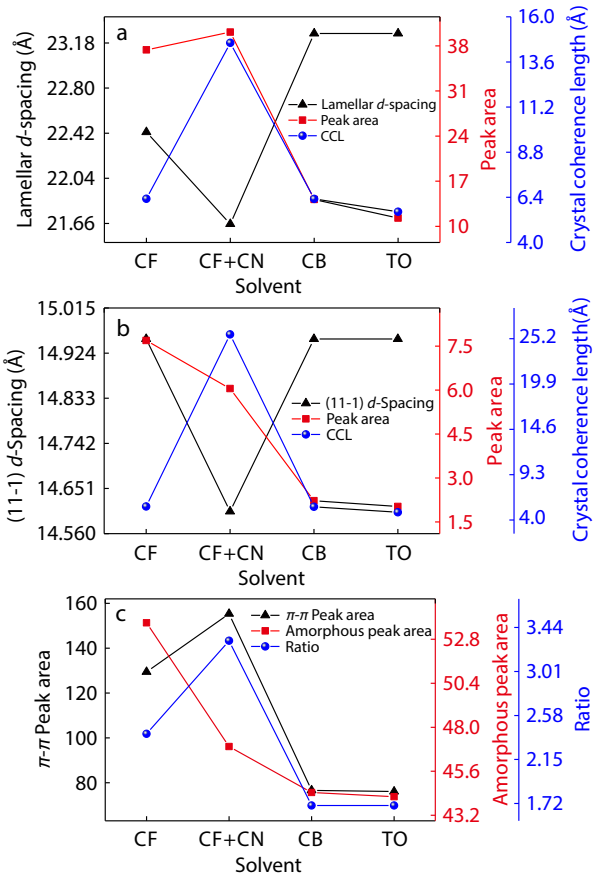

Fig. 5 Summary of fitting results for the GIWAXS data: *d*-spacing, peak area and CCL of (a) lamellar and (b) Y6 (11-1) of PM6:Y6 films processed with different solvents; (c) The *π*-*π* stacking peak areas, the amorphous peak areas and *π*-*π*/amorphous peak area ratios of PM6:Y6 blends processed with different solvents.

crystallinity in each blend. As shown in Fig. 5(c), the *π*-*π* stacking peak areas of CF/CN-, CF-, CB- and TO-processed films are 155.36, 129.42, 76.62 and 76.037, and the corresponding *π*-*π*/amorphous peak area ratios are 3.31, 2.4, 1.7 and 1.7, respectively. These results suggest less molecular order with incompact amorphous packing in CB- and TO-processed films. The low crystallinity and random orientation of CB- and TO-processed blends are detrimental to charge transport and lead to serious non-geminate recombination, which is the major origin of the lower OPV performances in comparison with the CF- and CF/CN-processed blends.

Atomic force microscopy (AFM) was used to study the surface morphology of PM6:Y6 blend films. The height and phase images are presented in Fig. 6. The root-mean-square roughness (RMS) values obtained from the height image increase from 1.5, 10.6, 12.9 and 13.5 nm for blends processed with CF, CF/CN, CB and TO, respectively. The smooth surface of the CF-processed film helps to build better contact with the upper electron transport layer, facilitating the charge extraction in devices. As shown in the phase images, both CF- and CF/CN-processed films show a fibrillar morphology, where the fibrils in the latter are more robust with larger length scale. When using the CB and TO as processing solvents, large-scale aggregates can be observed.

The interaction parameters and boiling points of different solvents play key roles in determining such differences in morphology. Hansen[43] and Van[44] solubility parameters of each material are calculated by group contribution methods (Table S4 in ESI). The solubility parameters resulted from the two methods are quite similar, and the Hansen solubility parameters were used to estimate the solvent-solute interactions: δ_{PM6}=21.21, δ_{Y6}=22.32, δ_{CF}=19, δ_{CN}=21.74, δ_{CB}=19.63, δ_{TO}=18.13. Such results suggest that PM6 and Y6 both have gradually increased solubility in TO, CF, CB and CN. The solvent-solute affinities could be described as interaction parameters calculated by $\chi_{ij} = \frac{v_i}{RT}(\delta_i - \delta_j)^2 + 0.34$, where v_i is molar volume of solvent, and the constant 0.34 represents entropic contribution. The calculated solvent-solute interaction parameters are: $\chi_{CF\text{-}PM6}$=0.504, $\chi_{CN\text{-}PM6}$=0.35, $\chi_{CB\text{-}PM6}$=0.439, $\chi_{TO\text{-}PM6}$=0.739, $\chi_{CF\text{-}Y6}$=0.710, $\chi_{CN\text{-}Y6}$=0.36, $\chi_{CB\text{-}Y6}$=0.628, $\chi_{TO\text{-}Y6}$=1.079 (Table S5 in ESI). The larger the interaction parameter indicates the more immiscibility of two components. The boiling points of the different solvents are also need to be taken into account for the analysis: 61.2 °C (CF), 263 °C (CN), 132.2 °C (CB) and 110.4 °C (TO), since higher boiling point solvent evaporates more slowly, leading to different kinetics of structural evolutions. The fast evaporation of CF helps to form a fibril-based phase separation with appropriate scale size. The addition of CN, which is a good solvent for both PM6 and Y6, coupled with its high boiling point, promoted the molecular rearrangement at the later stage of film drying, and thus, substantially causing an increase in the crystalline domain size that exceeds the exciton diffusion length. Both CB- and TO-processed films are of low crystallinity, implying that the large-scale aggregates are unlikely driven by crystallization. Decreased crystallization leads to increased amorphous molecules that will participate into the amorphous region, where possible liquid-liquid (L-L) decomposition[45] proceeds and is strongly influenced by compositional interactions. The low interaction parameters of CB with the solutes imply that solutes have good solubility in CB. Thus, low crystallinity and high boiling point will provide sufficient liquid-phase solutes under prolonged drying process, which allow for L-L phase separation, resulting in large-scale phase domains. Although evaporation of TO is faster than CB, Y6 shows poor solubility in TO due to the high interaction parameters. TO could easily induce Y6 aggregation, and thus, promoting formation of domains with hundreds of nanometers and a higher RMS value.

Therefore, a comprehensive analysis is presented to demonstrate the role of processing solvent on device performance, device physics, photophysics, and morphology of slot-die printed PM6:Y6 blend system. The CF-processed blends show the best performance, due to the combination of suppressed geminate and non-geminate recombination, fast exciton diffusion and hole transfer process, and high and balanced charge carrier mobilities. Morphology characterizations indicate that CF-processed blend shows a fibrillar network with good materials crystallization. For the CF/CN case, the host solvent CF helps to form the fibril morphology in the early stage, while the remaining CN substantially promotes molecular crystallization at the later stage of film drying, res-

https://doi.org/10.1007/s10118-022-2866-2

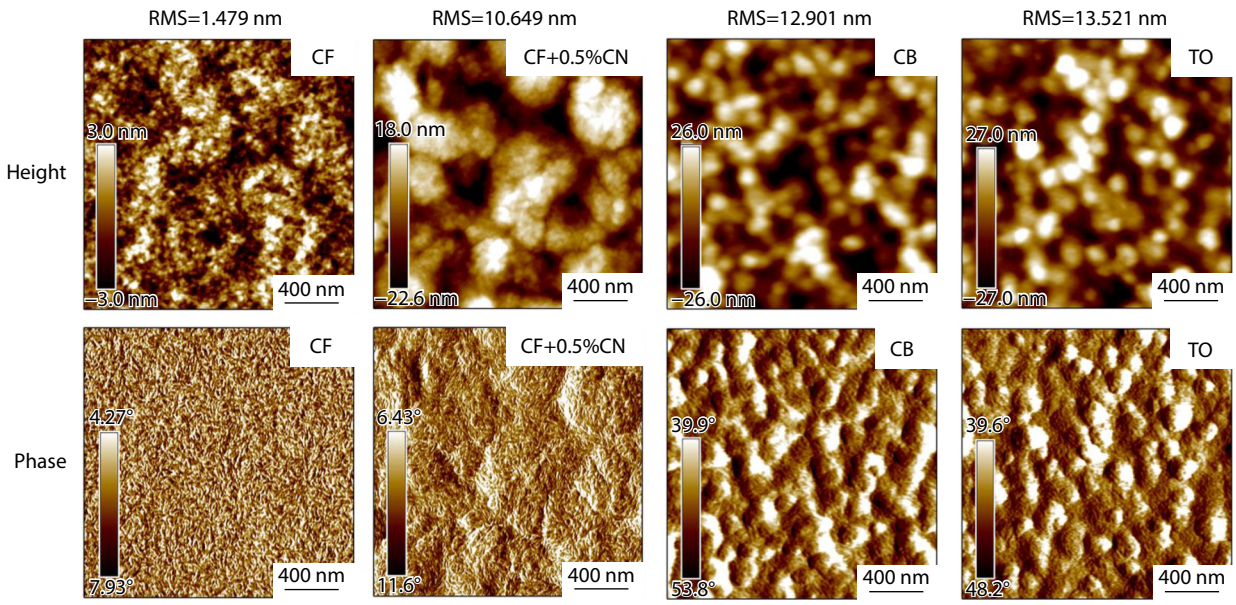

Fig. 6 AFM height and phase images of PM6:Y6 blend films processed by different solvents.

ulting in a large crystalline domain size. Such large phase separation leads to the low efficiency of photogenerated excitons diffusing to the interface and splitting, and also causes serious bimolecular recombination, and thus, decreasing the performance. It is found that Y6 shows low crystallinity in both CB and TO blends, which is unfavorable for charge transport, in consistent with the low charge carrier mobilities and increased recombination. Though these two solvents can provide longer time for molecular crystallization, the interactions between solvent and materials need to be considered, which may critically influence the crystallization rate. The low crystallinity of Y6 leaves more molecules to participate L-L demixing, forming large phase separation that causes serious exciton and non-geminate recombination, leading to a sharp drop in J_{SC} and FF. The poor solubility of Y6 in TO leads to evolve into large aggregates with hundreds of nanometers, showing the low hole transfer efficiency from Y6 to PM6 and the serious biomolecular and trap-assisted recombination, and ultimately, showing severe decrease of J_{SC} and FF. Further morphology optimization for CB- and TO-blends may be achievable by increasing the substrate temperature, which has proven to boost the crystallization rate and control the termination of film drying, and a higher crystallinity as well as improved device performance are expected.[6,7]

CONCLUSIONS

In summary, different processing solvents (CF, CF/CN, CB and TO) are employed to manipulate the film morphology of PM6:Y6 blends, and the role of processing solvent on morphology-function relations is studied. It is found that the morphology and device performance in slot-die printing are greatly influenced by solvent properties, including the effect of solvent on solutes crystallization, evaporation rate, and the interaction parameters with solutes. When the solutes have a strong tendency to crystallize in the solvent, such as CF, which can form inter-connected crystalline domains for efficient charge transport. Moreover, the collective effects of crystalline domains and amorphous mixing background need to be taken into account, and thus, the processing solvent should not induce over-crystallization during drying, such as the case of CF/CN. Therefore, the selection of an optimal processing solvent is prerequisite for fabricating a high-performance OPV device. Although how the processing solvent influences the crystallization kinetics is elusive so far, the evaporation rate of the solvent, which is determined by its boiling point and the substrate temperature, can be controlled to arrest the crystallization process at a certain time frame, which could help to generate a morphology with proper domain size and interface that are favorable to charge generation and transport. The low crystallinity of Y6 in CB-and TO-blends is attributed to the low crystallization rate in these solvents, leaving more amorphous molecules to participate the L-L demixing, which leads to large-scale amorphous aggregates, and thus, severe recombination loss as well as decrease in efficiency. Solvents with fast evaporation and good miscibility with solutes can obtain favorable phase separation and crystallization in slot-die printing. The best PCE of 16.22% is achieved by CF-processed PM6:Y6 blends, which is among highest efficiencies for slot-die printed OPV devices. Our results reveal new insights into morphology-function relations on the roles of processing solvents, providing guiding strategies to manipulate the morphology for high-efficiency printed devices.

NOTES

The authors declare no competing financial interest.

Electronic Supplementary Information

Electronic supplementary information (ESI) is available free of charge in the online version of this article at http://doi.org/10.1007/s10118-022-2866-2.

ACKNOWLEDGMENTS

This work was financially supported by the National Natural Science Foundation of China (Nos. 51973110, 21734009, 21905102 and 22109094), the Program of Shanghai Science and Technology Commission science and technology innovation action plan (Nos. 20ZR1426200, 20511103800, 20511103802 and 20511103803), the Natural Science Foundation of Shandong Province (No. ZR2019LFG005), the Key research project of Shandong Province (No. 2020CXGC010403), the Center of Hydrogen Science, Shanghai Jiao Tong University, China. GIWAXS was performed at beamline 7.3.3 at the Advanced Light Source, a U.S. DOE Office of Science User Facility under contract no. DE-AC02-05CH11231.

REFERENCES

1 Ng, L. W. T.; Lee, S. W.; Chang, D. W.; Hodgkiss, J. M.; Vak, D. Organic photovoltaics' new renaissance: advances toward roll-to-roll manufacturing of non-fullerene acceptor organic photovoltaics. *Adv. Mater. Technol.* **2022**, *7*, 2101556.
2 Luo, D.; Jang, W.; Babu, D.; Kim, M. S.; Wang, D. H.; Kyaw, A. K. K. Recent progress in organic solar cells based on non-fullerene acceptors: materials to devices. *J. Mater. Chem. A* **2022**, *10*, 3255–3295.
3 Sharma, T.; Mahajan, P.; Adil Afroz, M.; Singh, A.; Kumar Tailor, N.; Purohit, S.; Verma, S.; Padha, B.; Gupta, V.; Arya, S. Recent progress in advanced organic photovoltaics: emerging techniques and materials. *ChemSusChem* **2022**, *15*, e202101067.
4 Cui, Y.; Xu, Y.; Yao, H.; Bi, P.; Hong, L.; Zhang, J.; Zu, Y.; Zhang, T.; Qin, J.; Ren, J. Single-junction organic photovoltaic cell with 19% efficiency. *Adv. Mater.* **2021**, *33*, 2102420.
5 Chong, K.; Xu, X.; Meng, H.; Xue, J.; Yu, L.; Ma, W.; Peng, Q. Realizing 19. 05% efficiency polymer solar cells by progressively improving charge extraction and suppressing charge recombination. *Adv. Mater.* **2022**, *34*, 2109516.
6 Li, Y.; Liu, H.; Wu, J.; Tang, H.; Wang, H.; Yang, Q.; Fu, Y.; Xie, Z. Additive and high-temperature processing boost the photovoltaic performance of nonfullerene organic solar cells fabricated with blade coating and nonhalogenated solvents. *ACS Appl. Mater. Interfaces* **2021**, *13*, 10239–10248.
7 Zhao, H.; Naveed, H. B.; Lin, B.; Zhou, X.; Yuan, J.; Zhou, K.; Wu, H.; Guo, R.; Scheel, M. A.; Chumakov, A. Hot hydrocarbon-solvent slot-die coating enables high-efficiency organic solar cells with temperature-dependent aggregation behavior. *Adv. Mater.* **2020**, *32*, 2002302.
8 Xu, J.; Zhan, J.; Zhou, G.; Zhong, W.; Zhang, M.; Xue, X.; Zhu, L.; Leng, S.; Chen, J.; Zou, Y. Slot-die-coated organic solar cells optimized through multistep crystallization kinetics. *Sol. RRL* **2022**, *6*, 2100740.
9 Dong, S.; Jia, T.; Zhang, K.; Jing, J.; Huang, F. Single-component non-halogen solvent-processed high-performance organic solar cell module with efficiency over 14%. *Joule* **2020**, *4*, 2004–2016.
10 Xue, J.; Zhao, H.; Lin, B.; Wang, Y.; Zhu, Q.; Lu, G.; Wu, B.; Bi, Z.; Zhou, X.; Zhao, C. Nonhalogenated dual-slot-die processing enables high-efficiency organic solar cells. *Adv. Mater.* **2022**, *34*, 2202659.
11 Xue, J.; Naveed, H. B.; Zhao, H.; Lin, B.; Wang, Y.; Zhu, Q.; Wu, B.; Bi, Z.; Zhou, X.; Zhao, C. Kinetic processes of phase separation and aggregation behaviors in slot-die processed high efficiency Y6-based organic solar cells. *J. Mater. Chem. A* **2022**, *10*, 13439–13447.
12 Guo, S.; Wang, W.; Herzig, E. M.; Naumann, A.; Tainter, G.; Perlich, J.; Müller-Buschbaum, P. Solvent-morphology-property relationship of PTB7:PC71BM polymer solar cells. *ACS Appl. Mater. Interfaces* **2017**, *9*, 3740–3748.
13 An, K.; Zhong, W.; Ying, L.; Zhu, P.; Fan, B.; Li, Z.; Li, N.; Huang, F.; Cao, Y. Optimization of processing solvent and film morphology to achieve efficient non-fullerene polymer solar cells processed in air. *J. Mater. Chem. C* **2020**, *8*, 270–275.
14 Ye, L.; Xiong, Y.; Zhang, Q.; Li, S.; Wang, C.; Jiang, Z.; Hou, J.; You, W.; Ade, H. Surpassing 10% efficiency benchmark for nonfullerene organic solar cells by scalable coating in air from single nonhalogenated solvent. *Adv. Mater.* **2018**, *30*, 1705485.
15 Zhan, J.; Wang, L.; Zhang, M.; Zhu, L.; Hao, T.; Zhou, G.; Zhou, Z.; Chen, J.; Zhong, W.; Qiu, C. Manipulating crystallization kinetics of conjugated polymers in nonfullerene photovoltaic blends toward refined morphologies and higher performances. *Macromolecules* **2021**, *54*, 4030–4041.
16 McDowell, C.; Abdelsamie, M.; Toney, M. F.; Bazan, G. C. Solvent additives: key morphology-directing agents for solution-processed organic solar cells. *Adv. Mater.* **2018**, *30*, 1707114.
17 Chen, Y.; Zhang, X.; Zhan, C.; Yao, J. Origin of effects of additive solvent on film-morphology in solution-processed nonfullerene solar cells. *ACS Appl. Mater. Interfaces* **2015**, *7*, 6462–6471.
18 Zhang, L.; Xu, X.; Lin, B.; Zhao, H.; Li, T.; Xin, J.; Bi, Z.; Qiu, G.; Guo, S.; Zhou, K. Achieving balanced crystallinity of donor and acceptor by combining blade-coating and ternary strategies in organic solar cells. *Adv. Mater.* **2018**, *30*, 1805041.
19 Zhao, C.; Wang, J.; Zhao, X.; Du, Z.; Yang, R.; Tang, J. Recent advances, challenges and prospects in ternary organic solar cells. *Nanoscale* **2021**, *13*, 2181–2208.
20 Verploegen, E.; Mondal, R.; Bettinger, C. J.; Sok, S.; Toney, M. F.; Bao, Z. Effects of thermal annealing upon the morphology of polymer-fullerene blends. *Adv. Funct. Mater.* **2010**, *20*, 3519–3529.
21 Shin, P. K.; Kumar, P.; Kumar, A.; Kannappan, S.; Ochiai, S. Effects of organic solvents for composite active layer of PCDTBT/PC71BM on characteristics of organic solar cell devices. *Int. J. Photoenergy* **2014**, *2014*, 786468.
22 Ruderer, M. A.; Guo, S.; Meier, R.; Chiang, H. Y.; Körstgens, V.; Wiedersich, J.; Perlich, J.; Roth, S. V.; Müller-Buschbaum, P. Solvent-induced morphology in polymer-based systems for organic photovoltaics. *Adv. Funct. Mater.* **2011**, *21*, 3382–3391.
23 Zhu, L.; Zhang, M.; Zhou, G.; Hao, T.; Xu, J.; Wang, J.; Qiu, C.; Prine, N.; Ali, J.; Feng, W. Efficient organic solar cell with 16. 88% efficiency enabled by refined acceptor crystallization and morphology with improved charge transfer and transport properties. *Adv. Energy Mater.* **2020**, *10*, 1904234.
24 Kyaw, A. K. K.; Wang, D. H.; Gupta, V.; Leong, W. L.; Ke, L.; Bazan, G. C.; Heeger, A. J. Intensity dependence of current-voltage characteristics and recombination in high-efficiency solution-processed small-molecule solar cells. *ACS Nano* **2013**, *7*, 4569–4577.
25 Blom, P. W.; Mihailetchi, V. D.; Koster, L. J. A.; Markov, D. E. Device physics of polymer: fullerene bulk heterojunction solar cells. *Adv. Mater.* **2007**, *19*, 1551–1566.
26 Lin, H.; Chen, S.; Li, Z.; Lai, J. Y. L.; Yang, G.; McAfee, T.; Jiang, K.; Li, Y.; Liu, Y.; Hu, H. High-performance non-fullerene polymer solar cells based on a pair of donor-acceptor materials with complementary absorption properties. *Adv. Mater.* **2015**, *27*, 7299–7304.
27 Carbone, A.; Kotowska, B.; Kotowski, D. Space-charge-limited current fluctuations in organic semiconductors. *Phys. Rev. Lett.* **2005**, *95*, 236601.
28 Li, Z.; Jiang, K.; Yang, G.; Lai, J. Y. L.; Ma, T.; Zhao, J.; Ma, W.; Yan, H. Donor polymer design enables efficient non-fullerene organic solar cells. *Nat. Commun.* **2016**, *7*, 13094.
29 Bakulin, A. A.; Rao, A.; Pavelyev, V. G.; van Loosdrecht, P. H.;

Pshenichnikov, M. S.; Niedzialek, D.; Cornil, J.; Beljonne, D.; Friend, R. H. The role of driving energy and delocalized states for charge separation in organic semiconductors. *Science* **2012**, *335*, 1340–1344.
30 Wang, R.; Zhang, C.; Li, Q.; Zhang, Z.; Wang, X.; Xiao, M. Charge separation from an intra-moiety intermediate state in the high-performance PM6:Y6 organic photovoltaic blend. *J. Am. Chem. Soc.* **2020**, *142*, 12751–12759.
31 Zhou, G.; Ding, H.; Zhu, L.; Qiu, C.; Zhang, M.; Hao, T.; Feng, W.; Zhang, Y.; Zhu, H.; Liu, F. Photophysics, morphology and device performances correlation on non-fullerene acceptor based binary and ternary solar cells. *J. Energy Chem.* **2020**, *47*, 180–187.
32 Li, T.; Wang, K.; Cai, G.; Li, Y.; Liu, H.; Jia, Y.; Zhang, Z.; Lu, X.; Yang, Y.; Lin, Y. Asymmetric glycolated substitution for enhanced permittivity and ecocompatibility of high-performance photovoltaic electron acceptor. *JACS Au* **2021**, *1*, 1733–1742.
33 Koster, L. J. A.; Mihailetchi, V. D.; Ramaker, R.; Blom, P. W. Light intensity dependence of open-circuit voltage of polymer:fullerene solar cells. *Appl. Phys. Lett.* **2005**, *86*, 123509.
34 Schilinsky, P.; Waldauf, C.; Brabec, C. J. Recombination and loss analysis in polythiophene based bulk heterojunction photodetectors. *Appl. Phys. Lett.* **2002**, *81*, 3885–3887.
35 Foertig, A.; Rauh, J.; Dyakonov, V.; Deibel, C. Shockley equation parameters of P3HT:PCBM solar cells determined by transient techniques. *Phys. Rev. B* **2012**, *86*, 115302.
36 Lv, J.; Tang, H.; Huang, J.; Yan, C.; Liu, K.; Yang, Q.; Hu, D.; Singh, R.; Lee, J.; Lu, S. Additive-induced miscibility regulation and hierarchical morphology enable 17.5% binary organic solar cells. *Energy Environ. Sci.* **2021**, *14*, 3044–3052.
37 Maurano, A.; Shuttle, C. G.; Hamilton, R.; Ballantyne, A. M.; Nelson, J.; Zhang, W.; Heeney, M.; Durrant, J. R. Transient optoelectronic analysis of charge carrier losses in a selenophene/fullerene blend solar cell. *J. Phys. Chem. C* **2011**, *115*, 5947–5957.
38 Min, J.; Güldal, N. S.; Guo, J.; Fang, C.; Jiao, X.; Hu, H.; Heumüller, T.; Ade, H.; Brabec, C. J. Gaining further insight into the effects of thermal annealing and solvent vapor annealing on time morphological development and degradation in small molecule solar cells. *J. Phys. Chem. A* **2017**, *5*, 18101–18110.
39 Firdaus, Y.; Maffei, L. P.; Cruciani, F.; Müller, M. A.; Liu, S.; Lopatin, S.; Wehbe, N.; Ndjawa, G. O. N.; Amassian, A.; Laquai, F. Polymer main-chain substitution effects on the efficiency of nonfullerene bhj solar cells. *Adv. Energy Mater.* **2017**, *7*, 1700834.
40 Liu, Y.; Zhou, K.; Zhou, X.; Xue, W.; Bi, Z.; Wu, H.; Ma, Z.; Ma, W. Strengthening the intermolecular interaction of prototypical semicrystalline conjugated polymer enables improved photocurrent generation at the heterojunction. *Macromol. Rapid Commun.* **2022**, 2100871.
41 Xu, X.; Yu, L.; Yan, H.; Li, R.; Peng, Q. Highly efficient non-fullerene organic solar cells enabled by a delayed processing method using a non-halogenated solvent. *Energy Environ. Sci.* **2020**, *13*, 4381–4388.
42 Hu, Q.; Chen, W.; Yang, W.; Li, Y.; Zhou, Y.; Larson, B. W.; Johnson, J. C.; Lu, Y. H.; Zhong, W.; Xu, J. Improving efficiency and stability of perovskite solar cells enabled by a near-infrared-absorbing moisture barrier. *Joule* **2020**, *4*, 1575–1593.
43 Hansen, C. M. *Hansen solubility parameters: a user's handbook*. CRC Press: **2007**, p. 4.
44 Van Krevelen, D. W.; Te Nijenhuis, K. *Properties of polymers: their correlation with chemical structure; their numerical estimation and prediction from additive group contributions*. Elsevier: **2009**, p. 191.
45 Biernat, M.; Dąbczyński, P.; Biernat, P.; Rysz, J. Phase separation in PCDTBT:PCBM blends: from flory-huggins interaction parameters to ternary phase diagrams. *Chinese J. Polym. Sci.* **2020**, *38*, 1025–1033.

https://doi.org/10.1007/s10118-022-2866-2